Available online at www.sciencedirect.com
ScienceDirect
Trans. Nonferrous Met. Soc. China 32(2022) 2046−2060
Transactions of Nonferrous Metals Society of China
www.tnmsc.cn

Thermodynamic analysis of Na−S−Fe−H_2O system for Bayer process

Xue-jiao ZHOU, Fei TAN, Yong-li CHEN, Jian-guo YIN, Wen-tang XIA, Qing-yun HUANG, Xu-dong GAO

School of Metallurgical and Materials Engineering,
Chongqing University of Science and Technology, Chongqing 401331, China

Received 22 April 2021; accepted 24 December 2021

Abstract: Thermodynamic diagrams of Na−S−Fe−H_2O system were constructed to analyze the behavior of sulfur and iron in the Bayer process. After digestion, iron mainly exists as Fe_3O_4 and Fe_2O_3 in red mud, and partial iron transfers into solution as $Fe(OH)_3^-$, $HFeO_2^-$, $Fe(OH)_4^-$ and $Fe(OH)_4^{2-}$. The dominant species of sulfur is S^{2-}, followed by SO_4^{2-}, and then SO_3^{2-} and $S_2O_3^{2-}$. The thermodynamic analysis is consistent with the iron and sulfur species distribution in the solution obtained by experiments. When the temperature decreases, sulfur and iron can combine and precipitate. Controlling low potential and reducing temperature are beneficial to removing them from the solution. XRD patterns show that $NaFeS_2{\cdot}2H_2O$, FeS and FeS_2 widely appear in red mud and precipitates of pyrite and high-sulfur bauxite digestion solution. Thermodynamic analysis can be utilized to guide the simultaneous removal of sulfur and iron in the Bayer process.

Key words: high-sulfur bauxite; Na−S−Fe−H_2O system; thermodynamic analysis; simultaneous removal; sulfur; iron; Bayer process

1 Introduction

The phylogeny of the Chinese alumina industry is a development history to overcome the defects of diasporic bauxite. It requires higher temperatures (>513 K) and Na_2O_k concentrations (>240 g/L) to obtain a reasonable dissolution rate of Al_2O_3 in the digestion process [1]. Under such strong conditions, a large amount of sulfur and iron, which generally exists as pyrite (FeS_2) in bauxite, can transfer into the sodium aluminate solution as various ions, resulting in a series of notable adverse effects [2,3]. Interesting research has been devoted to the influence of sulfur on the iron content in Bayer liquor and emphasized that the high sulfur in bauxite caused the excessive iron concentration in sodium aluminate solution [4]. The industrial application of bauxite containing 0.81% sulfur to produce alumina supported this conclusion. With the accumulation of sulfur in Bayer liquor, the iron content of $Al(OH)_3$ was seriously exceeded, even making the color of the product $Al(OH)_3$ change from white to green [5,6]. Therefore, desulfurization is an essential prerequisite for the reasonable utilization of high-sulfur bauxite.

Our previous research discovered that the sulfur and iron in the solution could combine and precipitate when the temperature decreased. XRD patterns showed that $NaFeS_2{\cdot}2H_2O$ and FeS appeared in the red mud of high-sulfur bauxite [7]. Based on this phenomenon, we proposed a novel and effective technology to simultaneously remove sulfur and iron from sodium aluminate solution [8]. This innovative technology is related to the digestion and precipitation behavior of these two impurities at different temperatures. Thermodynamic analysis of Na−S−Fe−H_2O system provides a theoretical basis for the possible digestion mechanisms of sulfur and iron in alkali

Corresponding author: Yong-li CHEN, Tel: +86-23-65022425, E-mail: hubeichyl@163.com
DOI: 10.1016/S1003-6326(22)65929-6

solution, and serves as a guide for selecting and optimizing technological parameters of simultaneously removing these two impurities.

Much attention has been paid to thermodynamic diagram of Fe−S−H_2O system [9−19]. As a straightforward and effective method, ΔG−T diagram was usually applied to analyzing the effect of temperature on the dissolution behavior of sulfur in alkali solution [11−16]. Results showed that sulfur principally entered into the solution as S^{2-}, and others were S_2^{2-}, $S_2O_3^{2-}$, SO_4^{2-} and SO_3^{2-}. Iron primarily precipitated into the slag as Fe_2O_3 or Fe_3O_4, and a small amount of $Na_2[FeS_2(OH)_2]\cdot 2H_2O$ was formed if there was much sulfur in the solution. φ_h−pH diagrams of Fe−S−H_2O system at elevated temperatures were plotted to clarify the corrosion behavior of iron in the saltwater or to discuss the formation mechanism of FeS_2 in the submarine hydrothermal system [17−19]. The results illuminated that the predominant area of $Fe(OH)_3^-$ expanded, while the dominant regions of FeS_2, Fe_3O_4 and FeS shrunk with raising the temperature. WANG et al [20] adopted φ_h−pH diagram of ZnS−FeS−H_2O system at 423 K to investigate the acid leaching behavior of high-iron sphalerite. These Pourbaix diagrams above can provide theoretical support for desulfurization, because FeS, FeS_2 and ZnS are the predominant species in alkali solution. Several studies have been carried out to separate sulfur from sodium aluminate solution by adding iron or zinc [15,16,21−23]. It was found that S^{2-} could react with ZnO, Fe and $NaFeO_2$ to form ZnS, Na_3FeS_3 and $NaFeS_2\cdot 2H_2O$, and then it was transferred from the solution into the red mud.

However, nearly all the thermodynamic studies on sulfur and iron involve only a single procedure in the Bayer process. Few researches have been carried out to analyze the system behavior of these two impurities in the digestion and sedimentation process. Moreover, some critical special species, such as $NaFeS_2\cdot 2H_2O$ and $NaFeS_2$, are not clearly presented in the thermodynamic analysis. This work is focused on these problems and attempts to conduct comprehensive and systematic thermodynamic research on sulfur and iron removal. It is commonly known that thermodynamic diagrams, such as φ_h−pH diagram, lg c−pH diagram, speciation-pH/potential diagram and ΔG−T diagram, are widely used in the field of hydrometallurgy [11,24−26]. Various tools, such as PhreeqC, PhreePlot, HSC Chemistry and Factsage, have attracted much attention to plot these diagrams [25,27−29]. In this work, ΔG−T diagram and φ_h−pH diagram are constructed with the assistance of software Factsage 7.1 to analyze the dissolution behavior of FeS_2 in the Bayer digestion and the precipitation behavior of sulfur and iron in the sedimentation process, providing theoretical guidance for the simultaneous removal of these two impurities from sodium aluminate solution.

2 Thermodynamic analysis of Na−S−Fe−H_2O system for Bayer digestion

In Bayer digestion, the typical Na_2O_k concentrations are 120−140 g/L for gibbsite and 240−280 g/L for diaspore, respectively. Their pH values are higher than 14. That is to say, this process is not sensitive to the pH value exhibiting on the thermodynamic diagrams. Thus, $\Delta G_T^\Theta - T$ diagram is appropriately adopted to expound the dissolution behavior of FeS_2 in alkali solution.

2.1 Thermodynamic data and equations

The standard molar Gibbs free energy (G_T^Θ) of different species in Na−S−Fe−H_2O system [30,31] and the possible reactions of FeS_2 with Na_2O_k at the elevated temperature used to construct $\Delta G_T^\Theta - T$ diagram are listed in Appendix A and Table 1.

2.2 $\Delta G_T^\Theta - T$ diagram

Generally, the Bayer digestion temperature of bauxite is approximately 423−573 K. Consequently, the temperature of $\Delta G_T^\Theta - T$ diagram is controlled in this range.

Based on the data of Appendix A, ΔG_T^Θ values of the chemical reactions in Table 1 are calculated according to the following formula:

$$\Delta G_T^\Theta = \sum \nu_i G_{T,i}^\Theta$$

where ν_i is the stoichiometric coefficient of the substance involved in the reaction, which is positive for products and negative for reactants.

Due to a large number of the reactions in the Na−S−Fe−H_2O system, they are divided into four categories to clearly reflect the $\Delta G_T^\Theta - T$ relationship of each reaction in the temperature range of 423−573 K, as follows:

Table 1 Possible reactions of FeS_2 with Na_2O_k

Chemical reaction	No.	Chemical reaction	No.
$FeS_2+2OH^-=FeO+S_2^{2-}+H_2O$	(1)	$FeS_2+3OH^-=FeOH^++7/4S^{2-}+1/4SO_4^{2-}+H_2O$	(33)
$FeS_2+2OH^-=FeO+S^{2-}+S+H_2O$	(2)	$FeS_2+3OH^-=HFeO_2^-+S_2^{2-}+H_2O$	(34)
$FeS_2+7/2OH^-=FeO+3/2S^{2-}+1/4S_2O_3^{2-}+7/4H_2O$	(3)	$FeS_2+3OH^-=HFeO_2^-+S^{2-}+S+H_2O$	(35)
$FeS_2+4OH^-=FeO+5/3S^{2-}+1/3SO_3^{2-}+2H_2O$	(4)	$FeS_2+9/2OH^-=HFeO_2^-+3/2S^{2-}+1/4S_2O_3^{2-}+7/4H_2O$	(36)
$FeS_2+4OH^-=FeO+7/4S^{2-}+1/4SO_4^{2-}+2H_2O$	(5)	$FeS_2+5OH^-=HFeO_2^-+5/3S^{2-}+1/3SO_3^{2-}+2H_2O$	(37)
$FeS_2+2OH^-=Fe(OH)_2+S_2^{2-}$	(6)	$FeS_2+5OH^-=HFeO_2^-+7/4S^{2-}+1/4SO_4^{2-}+2H_2O$	(38)
$FeS_2+2OH^-=Fe(OH)_2+S^{2-}+S$	(7)	$FeS_2+OH^-=FeOH^{2+}+S^{2-}+1/2S_2^{2-}$	(39)
$FeS_2+7/2OH^-=Fe(OH)_2+3/2S^{2-}+1/4S_2O_3^{2-}+3/4H_2O$	(8)	$FeS_2+OH^-=FeOH^{2+}+3/2S^{2-}+1/2S$	(40)
$FeS_2+4OH^-=Fe(OH)_2+5/3S^{2-}+1/3SO_3^{2-}+H_2O$	(9)	$FeS_2+7/4OH^-=FeOH^{2+}+7/4S^{2-}+1/8S_2O_3^{2-}+3/8H_2O$	(41)
$FeS_2+4OH^-=Fe(OH)_2+7/4S^{2-}+1/4SO_4^{2-}+H_2O$	(10)	$FeS_2+2OH^-=FeOH^{2+}+11/6S^{2-}+1/6SO_3^{2-}+1/2H_2O$	(42)
$FeS_2+3/2OH^-=FeS+1/2S^{2-}+1/4S_2O_3^{2-}+3/4H_2O$	(11)	$FeS_2+2OH^-=FeOH^{2+}+15/8S^{2-}+1/8SO_4^{2-}+1/2H_2O$	(43)
$FeS_2+2OH^-=FeS+2/3S^{2-}+1/3SO_3^{2-}+H_2O$	(12)	$FeS_2+3OH^-=Fe(OH)_3^-+S_2^{2-}$	(44)
$FeS_2+2OH^-=FeS+3/4S^{2-}+1/4SO_4^{2-}+H_2O$	(13)	$FeS_2+3OH^-=Fe(OH)_3^-+S^{2-}+S$	(45)
$FeS_2+8/3OH^-=1/3Fe_3O_4+2/3S^{2-}+2/3S_2^{2-}+4/3H_2O$	(14)	$FeS_2+9/2OH^-=Fe(OH)_3^-+3/2S^{2-}+1/4S_2O_3^{2-}+3/4H_2O$	(46)
$FeS_2+8/3OH^-=1/3Fe_3O_4+4/3S^{2-}+2/3S+4/3H_2O$	(15)	$FeS_2+5OH^-=Fe(OH)_3^-+5/3S^{2-}+1/3SO_3^{2-}+H_2O$	(47)
$FeS_2+11/3OH^-=1/3Fe_3O_4+5/3S^{2-}+1/6S_2O_3^{2-}+11/6H_2O$	(16)	$FeS_2+5OH^-=Fe(OH)_3^-+7/4S^{2-}+1/4SO_4^{2-}+H_2O$	(48)
$FeS_2+4OH^-=1/3Fe_3O_4+16/9S^{2-}+2/9SO_3^{2-}+2H_2O$	(17)	$FeS_2+4OH^-=Fe(OH)_4^-+S^{2-}+1/2S_2^{2-}$	(49)
$FeS_2+4OH^-=1/3Fe_3O_4+11/6S^{2-}+1/6SO_4^{2-}+2H_2O$	(18)	$FeS_2+4OH^-=Fe(OH)_4^-+3/2S^{2-}+1/2S$	(50)
$FeS_2+3OH^-=1/2Fe_2O_3+S^{2-}+1/2S_2^{2-}+3/2H_2O$	(19)	$FeS_2+19/4OH^-=Fe(OH)_4^-+7/4S^{2-}+1/8S_2O_3^{2-}+3/8H_2O$	(51)
$FeS_2+3OH^-=1/2Fe_2O_3+3/2S^{2-}+1/2S+3/2H_2O$	(20)	$FeS_2+5OH^-=Fe(OH)_4^-+11/6S^{2-}+1/6SO_3^{2-}+1/2H_2O$	(52)
$FeS_2+15/4OH^-=1/2Fe_2O_3+7/4S^{2-}+1/8S_2O_3^{2-}+15/8H_2O$	(21)	$FeS_2+5OH^-=Fe(OH)_4^-+15/8S^{2-}+1/8SO_4^{2-}+1/2H_2O$	(53)
$FeS_2+4OH^-=1/2Fe_2O_3+11/6S^{2-}+1/6SO_3^{2-}+2H_2O$	(22)	$FeS_2+4OH^-=Fe(OH)_4^{2-}+S_2^{2-}$	(54)
$FeS_2+4OH^-=1/2Fe_2O_3+15/8S^{2-}+1/8SO_4^{2-}+2H_2O$	(23)	$FeS_2+4OH^-=Fe(OH)_4^{2-}+S^{2-}+S$	(55)
$FeS_2+3OH^-=Fe(OH)_3+S^{2-}+1/2S_2^{2-}$	(24)	$FeS_2+11/2OH^-=Fe(OH)_4^{2-}+3/2S^{2-}+1/4S_2O_3^{2-}+3/4H_2O$	(56)
$FeS_2+3OH^-=Fe(OH)_3+3/2S^{2-}+1/2S$	(25)	$FeS_2+6OH^-=Fe(OH)_4^{2-}+5/3S^{2-}+1/3SO_3^{2-}+H_2O$	(57)
$FeS_2+15/4OH^-=Fe(OH)_3+7/4S^{2-}+1/8S_2O_3^{2-}+3/8H_2O$	(26)	$FeS_2+6OH^-=Fe(OH)_4^{2-}+7/4S^{2-}+1/4SO_4^{2-}+H_2O$	(58)
$FeS_2+4OH^-=Fe(OH)_3+11/6S^{2-}+1/6SO_3^{2-}+1/2H_2O$	(27)	$FeS_2+2OH^-=Fe(OH)_2^++S^{2-}+1/2S_2^{2-}$	(59)
$FeS_2+4OH^-=Fe(OH)_3+15/8S^{2-}+1/8SO_4^{2-}+1/2H_2O$	(28)	$FeS_2+2OH^-=Fe(OH)_2^++3/2S^{2-}+1/2S$	(60)
$FeS_2+OH^-=FeOH^++S_2^{2-}$	(29)	$FeS_2+11/4OH^-=Fe(OH)_2^++7/4S^{2-}+1/8S_2O_3^{2-}+3/8H_2O$	(61)
$FeS_2+OH^-=FeOH^++S^{2-}+S$	(30)	$FeS_2+3OH^-=Fe(OH)_2^++11/6S^{2-}+1/6SO_3^{2-}+1/2H_2O$	(62)
$FeS_2+5/2OH^-=FeOH^++3/2S^{2-}+1/4S_2O_3^{2-}+3/4H_2O$	(31)	$FeS_2+3OH^-=Fe(OH)_2^++15/8S^{2-}+1/8SO_4^{2-}+1/2H_2O$	(63)
$FeS_2+3OH^-=FeOH^++5/3S^{2-}+1/3SO_3^{2-}+H_2O$	(32)		

(1) ΔG_T^Θ values are mainly negative, and iron occurs in the form of solid phases after reactions.

(2) ΔG_T^Θ values are primarily positive, and iron exists as solid phases after reactions.

(3) ΔG_T^Θ values are partially negative, and iron occurs in the form of ions after reactions.

(4) ΔG_T^Θ values are basically positive, and iron exists as ions after reactions.

According to the calculation assisted with software Factsage 7.1, $\Delta G_T^\Theta - T$ curves of the Reactions (1)−(53) are drawn to discuss the effect of temperature on the dissolution of FeS_2 in alkali solution, as shown in Fig. 1.

In the temperature range of 423−573 K, FeS_2 can react with Na_2O_k to generate a series of solid and ionic substances, as shown in Fig. 1(a). Raising

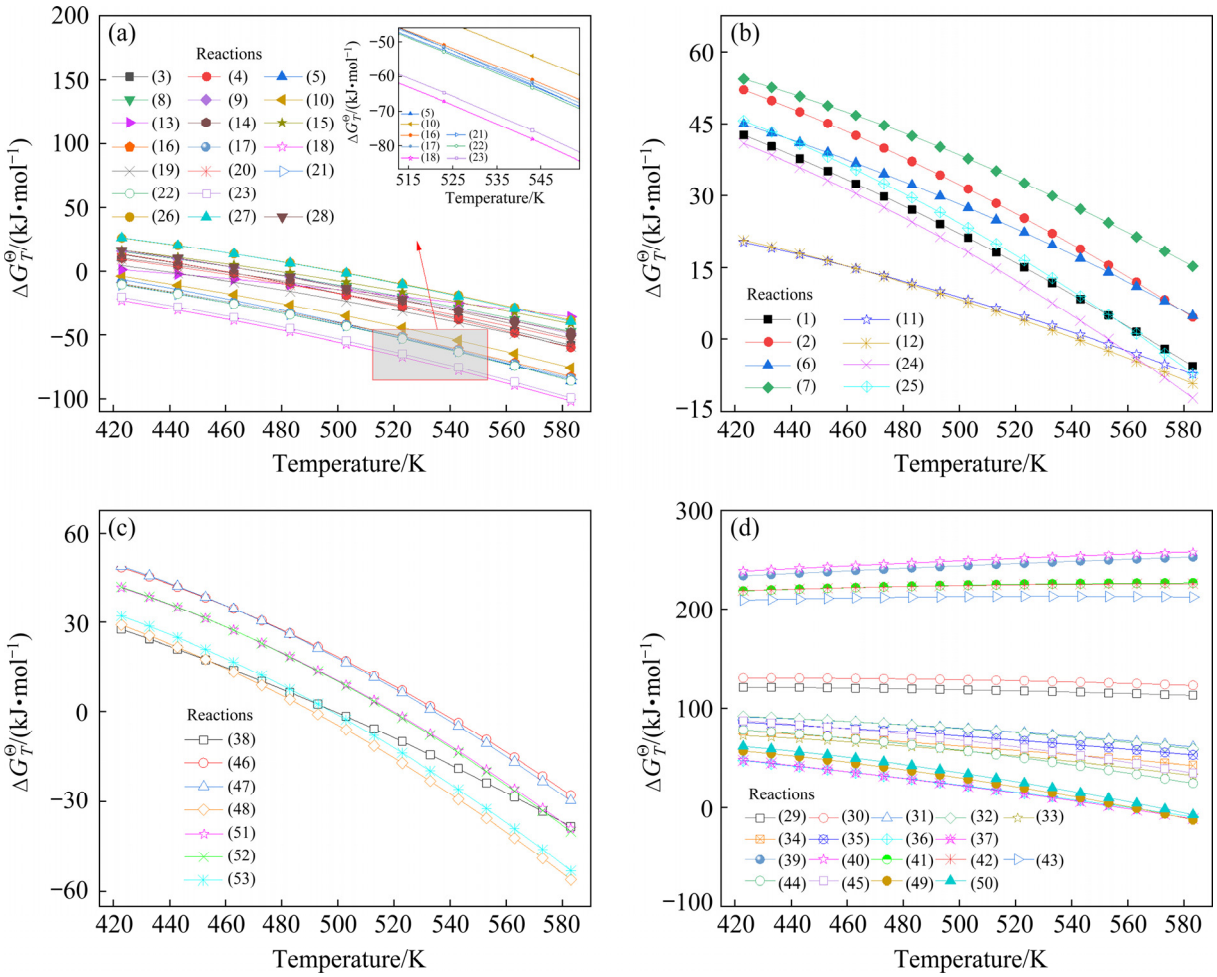

Fig. 1 $\Delta G_T^{\Theta}-T$ curves of different reactions: (a) Type (1); (b) Type (2); (c) Type (3); (d) Type (4)

the temperature is conducive to the decomposition of FeS_2. The partial enlarged view of Fig. 1(a) demonstrates that in 513−553 K range, $\Delta G_{T,(18)}^{\Theta} < \Delta G_{T,(23)}^{\Theta} < \Delta G_{T,(22)}^{\Theta} < \Delta G_{T,(21)}^{\Theta} / \Delta G_{T,(5)}^{\Theta} < \Delta G_{T,(17)}^{\Theta} < \Delta G_{T,(16)}^{\Theta} < \Delta G_{T,(10)}^{\Theta} < 0$. This means that these reactions prefer to happen. According to the principle of minimum Gibbs energy and stoichiometric coefficients of reactions, iron usually transfers into the slag in the form of Fe_3O_4 and Fe_2O_3, then $Fe(OH)_3$, FeO, $Fe(OH)_2$ and FeS. However, sulfur chiefly enters in the solution as S^{2-}, attributed to the fact that the apparent valence of sulfur in FeS_2 is negative, followed by SO_4^{2-}, and finally SO_3^{2-} and $S_2O_3^{2-}$.

The reactions in Fig. 1(b) are hardly conducted from the perspective of thermodynamics.

ΔG_T^{Θ} values of the reactions in Fig. 1(c) vary markedly with temperatures, and they are all negative above 543 K. Consequently, aqueous Fe(II) and Fe(III) species, such as $Fe(OH)_3^-$, $Fe(OH)_4^-$, and $HFeO_2^-$, can be formed. By further observation, Reaction (48) is preferred to happen in Bayer digestion of diasporic bauxite (T>513 K), and then Reaction (53). It is manifested that the iron transfers into the solution primarily in the form of $Fe(OH)_3^-$, followed by $Fe(OH)_4^-$, and the dominant species of sulfur is also S^{2-} with a small amount of SO_4^{2-} according to the stoichiometric coefficients of these two reactions.

Figure 1(d) shows that when FeS_2 is decomposed by Na_2O_k, ΔG_T^{Θ} values of these reactions are basically positive at the given temperatures and it is almost impossible to generate $FeOH^+$ and $FeOH^{2+}$.

In addition, it is unfortunate that thermodynamic data of $Fe(OH)_4^{2-}$ and $Fe(OH)^{2+}$ at elevated temperatures have not been found. Thus, only $\Delta G_{298\ K}^{\Theta}$ values of Reactions (54)−(63) (see Table 1) are calculated in this work. The results are presented in Table 2.

Table 2 $\Delta G^{\Theta}_{298\,K}$ values of Reactions (54)−(63)

Reaction	(54)	(55)	(56)	(57)	(58)	(59)	(60)	(61)	(62)	(63)
$\Delta G^{\Theta}_{298\,K}$/(kJ·mol^{-1})	92.66	99.35	70.74	71.94	55.10	146.76	150.10	135.79	136.39	127.97

Table 2 states that it is unrealistic to form $Fe(OH)_4^{2-}$ and $Fe(OH)^{2+}$ at 298 K. Nevertheless, increasing the temperature is usually beneficial to reducing ΔG_T^{Θ} values of the digestion reactions. Compared to Reactions (38), (46) and (48), it can be inferred that Reaction (58) may occur automatically at the digestion temperature of diasporic bauxite, and it is possible to generate $Fe(OH)_4^{2-}$, S^{2-} and SO_4^{2-}. These conclusions are in good agreement with previous research [32]. They found that when the temperature was achieved to 423 K, $Fe(OH)_4^-$, $Fe(OH)_4^{2-}$, FeO_4^{2-} and $Fe(OH)_3^-$ could be stable in alkali solution. In this research, FeO_4^{2-} is out of our consideration due to the actual situation of this system.

In summary, when FeS_2 reacts with Na_2O_k, iron prefers to enter in the slag mainly as Fe_3O_4 and Fe_2O_3 with a certain amount of $Fe(OH)_3$, $Fe(OH)_2$, FeS, etc. Meanwhile, a part of iron transfers into the solution as $Fe(OH)_3^-$, $HFeO_2^-$, $Fe(OH)_4^-$, $Fe(OH)_4^{2-}$, in which Fe(II) is dominant. Sulfur principally moves into the solution as ions, and the predominant species is S^{2-}, followed by SO_4^{2-}, and then SO_3^{2-} and $S_2O_3^{2-}$.

3 Thermodynamic analysis of Na−S−Fe−H_2O system for sedimentation process

Compared with the Bayer digestion, temperature and Na_2O_k concentration decrease in the sedimentation process, which is conducive to the precipitation of sulfur and iron. In the light of this characteristic, our previous research achieved the purpose of removing these two impurities before the seed decomposition of sodium aluminate solution [8]. Thermodynamic analysis of sulfur and iron in solution at 373 and 298 K is facilitated to clarify the predominant region and occurrence state of their different species.

3.1 φ_h−pH diagram

The reactions and thermodynamic equations (see Appendix B) calculated according to the data in Appendix A are used to construct the φ_h−pH diagram of S−Fe−H_2O system. Considering the preparation conditions of sulfur−iron seed and the fact that there are species of SO_3^{2-} and $S_2O_3^{2-}$ in sodium aluminate solution [13−16,23], Pourbaix diagrams at different temperatures and activities with $f(H_2)=f(O_2)=1.01\times10^5$ Pa are plotted, as shown in Fig. 2. The dash-dot lines define the boundaries of equal distribution between two dissolved species in adjacent areas, and the solid lines are served to describe the solid phases that occurred on one or both sides. Yellow lines are used to highlight the species distribution of sulfur. The area between the blue lines represents the stability domain of water, in which the dotted Line a describes the equilibrium between H_2O and O_2, and the dotted Line b corresponds to the H^+/H_2 equilibrium.

Figures 2(a−d) reveal that the dominant sulfur species are S^{2-}, HS^- and SO_4^{2-} at pH>7. HS^- converts into S^{2-} at higher pH and temperature. Therefore, in alumina production, sulfur prefers to occur as S^{2-} and SO_4^{2-}, which is in good agreement with the observation from Fig. 1. If the sulfate species are neglected, some metastable sulfur ions, such as SO_3^{2-}, $S_2O_3^{2-}$, $S_2O_8^{2-}$ would be favored to appear in the strong alkali solution.

While adding iron to this system, it is worth mentioning that at low potentials, a part of sulfur ions may be converted into sulfur-iron solids, such as FeS_2 and FeS. This means that the iron phases in seed slurry can strengthen the desulfurization by reaction crystallization. Lower temperature and higher activity provide an opportunity for enlarging their predominance area. Moreover, the metastable sulfur ions may contribute to expanding the dominant regions of these sulfur−iron solids.

In the view of the above discussion and analysis, the sulfur−iron seed should be prepared at room temperature with high concentration. Furthermore, it is also important to point out that the sulfur−iron solids are usually located in a low potential of S−Fe−H_2O system. Therefore, a reduction process of converting high-valence sulfur to low-valence sulfur may be a potential technology to remove sulfur from the solution. Adding reductants to react with $S_2O_3^{2-}$, SO_3^{2-}, SO_4^{2-} to form S^{2-} in Bayer digestion process has been confirmed as an effective desulfurization method [16,33], but a comprehensive and systematic work is still needed.

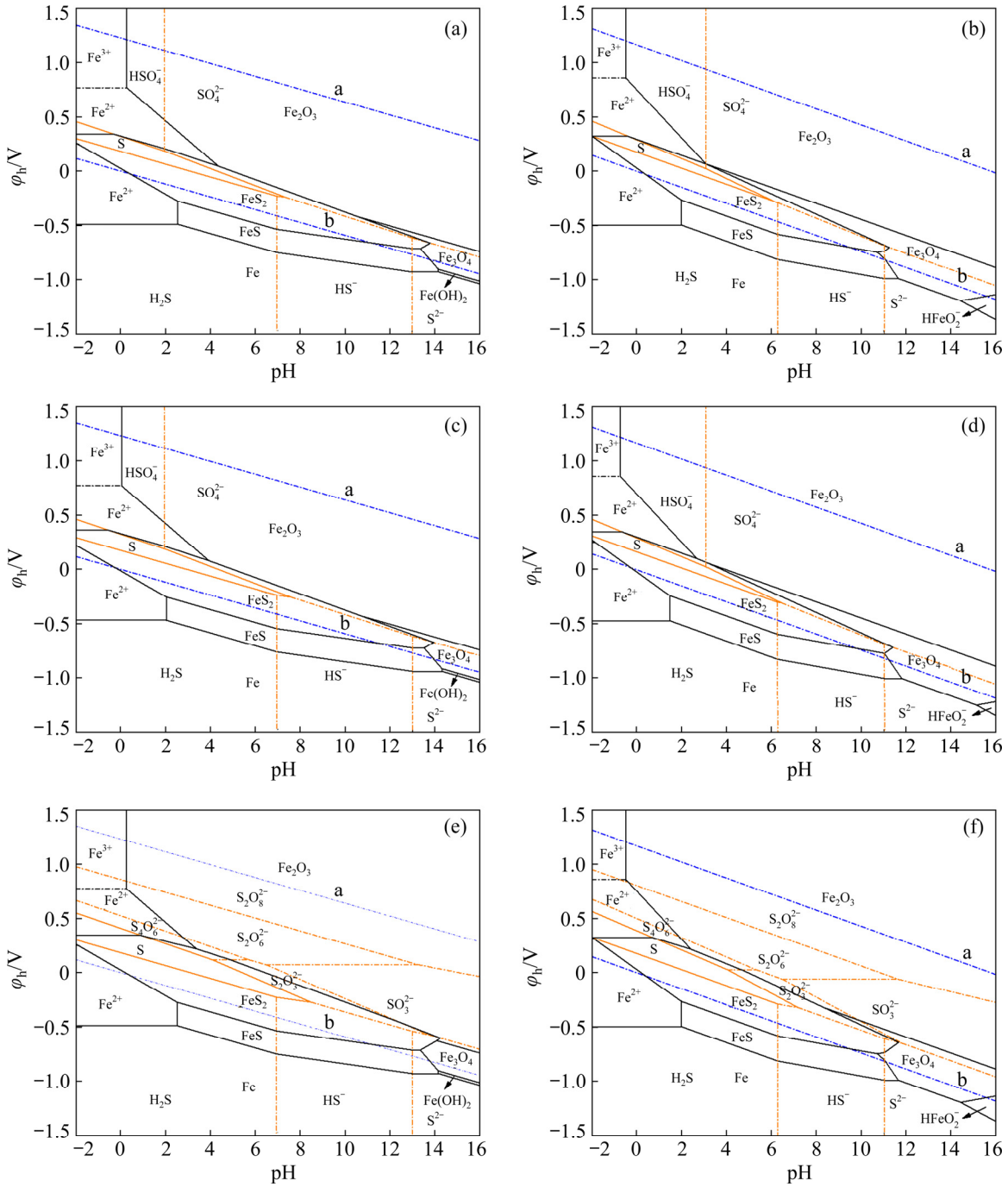

Fig. 2 φ_h–pH diagrams of S−Fe−H_2O system: (a) 298 K, a_{Fe}=0.002 mol/L, a_S=0.05 mol/L; (b) 373 K, a_{Fe}=0.002 mol/L, a_S=0.05 mol/L; (c) 298 K, a_{Fe}=0.01 mol/L, a_S=0.1 mol/L; (d) 373 K, a_{Fe}=0.01 mol/L, a_S=0.1 mol/L; (e) 298 K, a_{Fe}=0.002 mol/L, a_S=0.05 mol/L, without considering sulfate species; (f) 373 K, a_{Fe}=0.002 mol/L, a_S=0.05 mol/L, without considering sulfate species (a_{Fe} and a_S are the concentrations of dissolved iron and sulfur ions, respectively)

3.2 Thermodynamic calculations for special species

During the thermodynamic calculations of desulfurization, it is essential to focus on $NaFeS_2$ and $NaFeS_2{\cdot}2H_2O$, which usually emerge in red mud. Researchers have noticed these two species. However, because of the lack of data, they only calculated with valuation [12,23,33]. Up to date, there are only experimental data of these two substances at 298 K in the literature [34], and the values are different from those in Appendix A. Consequently, the data of the same series are adopted, as shown in Appendix C [34−37]. Possible reactions and their relevant $\Delta G^{\Theta}_{f,298\ K}$ to form $NaFeS_2$ and $NaFeS_2{\cdot}2H_2O$

are listed in Table 3 and Fig. 3.

Results in Fig. 3 imply that $NaFeS_2$ and $NaFeS_2·2H_2O$ can be generated at 298 K. By comparing $\Delta G^{\Theta}_{f,298\ K}$ values of these two species, it is evident that sulfur and iron prefer to form $NaFeS_2·2H_2O$ instead of $NaFeS_2$, which have been confirmed by the experiments [12,23]. In addition, it is meaningful to note that sulfur ions may react with $Fe(OH)_3$ or $NaFeO_2$ in seed to form $NaFeS_2·2H_2O$ and $NaFeS_2$. FeS_2 and FeS can also be generated by reactions of sulfur ions with iron-containing phases, as exhibited in Fig. 2. This means that combining the effect of induced crystallization and reactive crystallization can strengthen the removal of sulfur and iron from the digestion solution of high-sulfur bauxite.

4 Experimental results

4.1 Materials

Bauxite used in this work was derived from Nanchuan of Chongqing, China. Its characteristics were analyzed by XRF (PW2403, PANalytical B.V.), carbon−sulfur analyzer (TL851−5A, Lida Instrment), XRD (Smartlab−9, Rigaku, Japan) and SEM (JSM−7800F, Japan) [8]. Tables 4 and 5 revealed that it was a low-grade (A/S=3.34) [38] and high-sulfur (S>0.7%) diasporic bauxite. Figures 4 and 5 and Table 5 suggested that the main sulfur phase was FeS_2.

Table 3 Possible reactions to form $NaFeS_2$ and $NaFeS_2·2H_2O$

Chemical reaction	No.	Chemical reaction	No.
$Na^+ + Fe(OH)_3^- + 15/8S^{2-} + 1/8SO_4^{2-} + 1/2H_2O = NaFeS_2 + 4OH^-$	(1′)	$Na^+ + Fe(OH)_3^- + 15/8S^{2-} + 1/8SO_4^{2-} + 5/2H_2O = NaFeS_2·2H_2O + 4OH^-$	(16′)
$Na^+ + Fe(OH)_3^- + 11/6S^{2-} + 1/6SO_3^{2-} + 1/2H_2O = NaFeS_2 + 4OH^-$	(2′)	$Na^+ + Fe(OH)_3^- + 11/6S^{2-} + 1/6SO_3^{2-} + 5/2H_2O = NaFeS_2·2H_2O + 4OH^-$	(17′)
$Na^+ + Fe(OH)_3^- + 7/4S^{2-} + 1/8S_2O_3^{2-} + 3/8H_2O = NaFeS_2 + 15/4OH^-$	(3′)	$Na^+ + Fe(OH)_3^- + 7/4S^{2-} + 1/8S_2O_3^{2-} + 19/8H_2O = NaFeS_2·2H_2O + 15/4OH^-$	(18′)
$Na^+ + Fe(OH)_4^{2-} + 15/8S^{2-} + 1/8SO_4^{2-} + 1/2H_2O = NaFeS_2 + 5OH^-$	(4′)	$Na^+ + Fe(OH)_4^{2-} + 15/8S^{2-} + 1/8SO_4^{2-} + 5/2H_2O = NaFeS_2·2H_2O + 5OH^-$	(19′)
$Na^+ + Fe(OH)_4^{2-} + 11/6S^{2-} + 1/6SO_3^{2-} + 1/2H_2O = NaFeS_2 + 5OH^-$	(5′)	$Na^+ + Fe(OH)_4^{2-} + 11/6S^{2-} + 1/6SO_3^{2-} + 5/2H_2O = NaFeS_2·2H_2O + 5OH^-$	(20′)
$Na^+ + Fe(OH)_4^{2-} + 7/4S^{2-} + 1/8S_2O_3^{2-} + 3/8H_2O = NaFeS_2 + 19/4OH^-$	(6′)	$Na^+ + Fe(OH)_4^{2-} + 7/4S^{2-} + 1/8S_2O_3^{2-} + 19/8H_2O = NaFeS_2·2H_2O + 19/4OH^-$	(21′)
$Na^+ + HFeO_2^- + 15/8S^{2-} + 1/8SO_4^{2-} + 3/2H_2O = NaFeS_2 + 4OH^-$	(7′)	$Na^+ + HFeO_2^- + 15/8S^{2-} + 1/8SO_4^{2-} + 7/2H_2O = NaFeS_2·2H_2O + 4OH^-$	(22′)
$Na^+ + HFeO_2^- + 11/6S^{2-} + 1/6SO_3^{2-} + 3/2H_2O = NaFeS_2 + 4OH^-$	(8′)	$Na^+ + HFeO_2^- + 11/6S^{2-} + 1/6SO_3^{2-} + 7/2H_2O = NaFeS_2·2H_2O + 4OH^-$	(23′)
$Na^+ + HFeO_2^- + 7/4S^{2-} + 1/8S_2O_3^{2-} + 11/8H_2O = NaFeS_2 + 15/4OH^-$	(9′)	$Na^+ + HFeO_2^- + 7/4S^{2-} + 1/8S_2O_3^{2-} + 27/8H_2O = NaFeS_2·2H_2O + 15/4OH^-$	(24′)
$Na^+ + FeO_2^{2-} + 15/8S^{2-} + 1/8SO_4^{2-} + 5/2H_2O = NaFeS_2 + 5OH^-$	(10′)	$Na^+ + FeO_2^{2-} + 15/8S^{2-} + 1/8SO_4^{2-} + 9/2H_2O = NaFeS_2·2H_2O + 5OH^-$	(25′)
$Na^+ + FeO_2^{2-} + 11/6S^{2-} + 1/6SO_3^{2-} + 5/2H_2O = NaFeS_2 + 5OH^-$	(11′)	$Na^+ + FeO_2^{2-} + 11/6S^{2-} + 1/6SO_3^{2-} + 9/2H_2O = NaFeS_2·2H_2O + 5OH^-$	(26′)
$Na^+ + FeO_2^{2-} + 7/4S^{2-} + 1/8S_2O_3^{2-} + 19/8H_2O = NaFeS_2 + 19/4OH^-$	(12′)	$Na^+ + FeO_2^{2-} + 7/4S^{2-} + 1/8S_2O_3^{2-} + 35/8H_2O = NaFeS_2·2H_2O + 19/4OH^-$	(27′)
$Na^+ + Fe(OH)_4^- + 2S^{2-} = NaFeS_2 + 4OH^-$	(13′)	$Na^+ + Fe(OH)_4^- + 2S^{2-} + 2H_2O = NaFeS_2·2H_2O + 4OH^-$	(28′)
$Na^+ + Fe(OH)_3 + 2S^{2-} = NaFeS_2 + 3OH^-$	(14′)	$Na^+ + Fe(OH)_3 + 2S^{2-} + 2H_2O = NaFeS_2·2H_2O + 3OH^-$	(29′)
$NaFeO_2 + 2S^{2-} + 2H_2O = NaFeS_2 + 4OH^-$	(15′)	$NaFeO_2 + 2S^{2-} + 4H_2O = NaFeS_2·2H_2O + 4OH^-$	(30′)

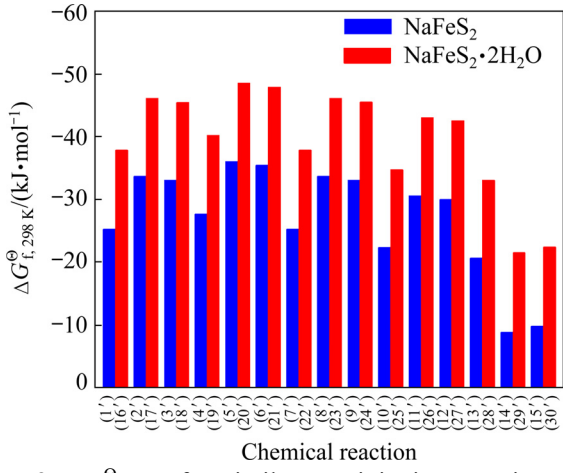

Fig. 3 $\Delta G^{\Theta}_{f,298\ K}$ for similar precipitation reactions of $NaFeS_2{\cdot}2H_2O$ and $NaFeS_2$

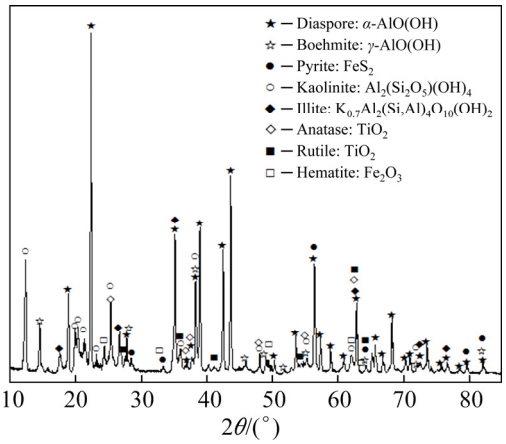

Fig. 4 XRD pattern of bauxite

Table 4 Chemical components of bauxite (wt.%)

Al_2O_3	SiO_2	Fe_2O_3	TiO_2	K_2O
59.62	17.84	1.82	2.89	0.83
Na_2O	CaO	MgO	S_{Total}	C_{Total}
0.17	0.14	0.19	0.88	0.29

Table 5 Mineral phases of bauxite (wt.%)

Diaspore	Boehmite	Kaolinite	Illite
44	8	31	8
Anatase	Rutile	Pyrite	Hematite
2.4	0.5	1.2	1

4.2 Experiment

Digestion of the bauxite was performed in a lifting autoclave, which consists of the reactor and control system. The main components of the reactor include the stirring device, cooling system and safety valve, etc. The autoclave cover, body and parts contacted with the medium are made of 316L stainless steel. The control system adopts an intelligent digital control instrument. The Bayer digestion was controlled as follows: 260 g/L Na_2O_k, temperature 543 K, agitation speed 100 r/min and reaction time 2 h. After digestion, the slurry was quickly separated by vacuum filtration. Then, the filtrate stood at room temperature to study the crystallization behavior of sulfur and iron in the

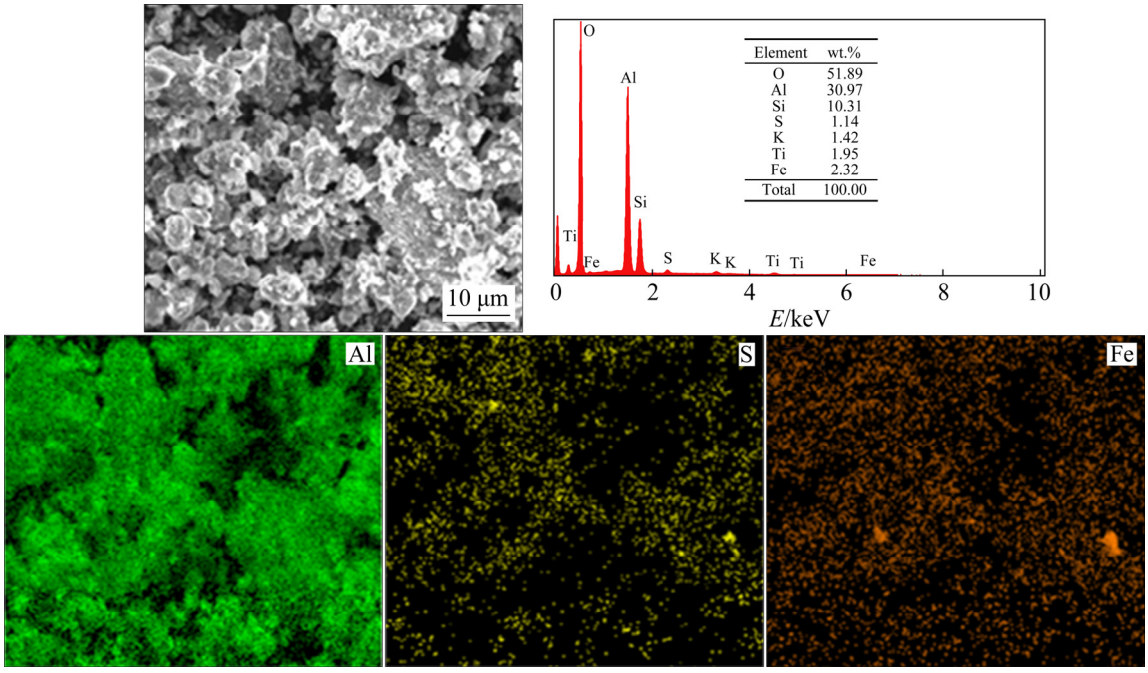

Fig. 5 Elemental mapping of bauxite

sodium aluminate solution. During the standing process, the conductivity of solution was monitored online with a conductivity meter (DDSJ−318, INESA). Sulfur, iron and sodium contents in the solution were determined by barium sulfate gravimetric method, iodometry, o-phenanthroline spectrophotometry (TU−1810, PERSEE) and AAS method (TAS−986, PERSEE) [6,39,40]. The red mud and the precipitates were analyzed by XRD, SEM, XRF and carbon−sulfur analyzer.

4.3 Leachate of high-sulfur bauxite

The analysis results of the leachate are given in Table 6.

Table 6 Sulfur and iron contents of different species in sodium aluminate solution

Species	Concentration/(mg·L^{-1})	Percentage/%
S^{2-}	1363	83.96
SO_4^{2-}	127.6	7.86
SO_3^{2-}	109.2	6.73
$S_2O_3^{2-}$	23.5	1.45
S_{Total}	1623.3	100
Fe(II)	121.3	91.41
Fe(III)	11.4	8.59
Fe_{Total}	132.7	100

T_S: Total sulfur content in solution; T_{Fe}: Total iron content in solution

Table 6 shows that the dominant species of sulfur is S^{2-}, which has exceeded 80% of the total sulfur content, followed by SO_4^{2-}, SO_3^{2-}, and then $S_2O_3^{2-}$. More than 90% of iron exists as Fe(II). These findings are coincident with the calculation in Figs. 1 and 2 and the previous results reported in the literatures [13,14,41,42].

S^{2-} is highly corrosive to the production equipment. After six months, obvious corrosion trace was distinctly observed in the autoclave liner, as displayed in Fig. 6.

Figure 6 manifests that the autoclave inner was corroded severely. Pitting corrosion could be found at the bottom of the autoclave inner. Radiation cracks and scaly corrosion primarily emerged from the upper middle of the liner to the liquid level line (white circle). Porphyritic corrosion was prominent at the lower middle of the autoclave inner. This phenomenon has attracted extensive attention, and considerable research efforts have been devoted to studying the corrosion behavior of S^{2-} on steel [43−46]. It was considered that steel would be seriously corroded by sulfur, especially S^{2-}, and oxides were formed with a loose structure. Raising temperature would accelerate the corrosion of steel surfaces [47]. Therefore, in the desulfurization of Bayer digestion, it is necessary and meaningful to remove S^{2-} [13−16,23].

Besides, more details in Table 6 manifest that the total iron content in the sodium aluminate solution was as high as 132.7 mg/L, far exceeding the iron content of the normal alumina production process, which is usually about 20−30 mg/L [48]. This phenomenon is generally attributed to the excessive sulfur content, which has been concerned by many scholars [4,5,16]. Consequently, to rationally develop and utilize the high-sulfur bauxite, it is necessary to solve the problem of high sulfur and iron in sodium aluminate solution.

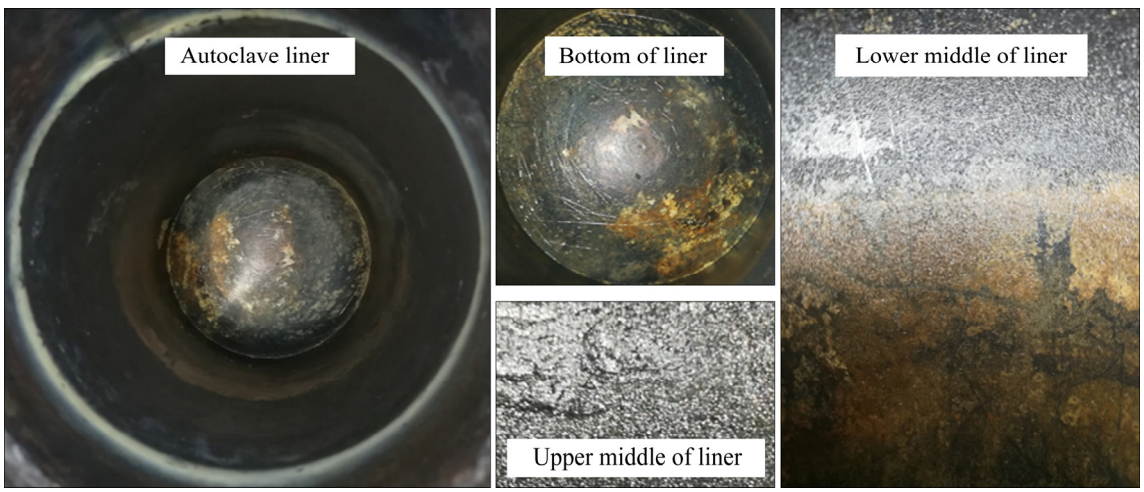

Fig. 6 Corrosion photos of autoclave

4.4 Crystallization behavior of sulfur−iron compounds in red mud

The chemical composition of the red mud is displayed in Table 7.

Table 7 Chemical components of red mud (wt.%)

Al_2O_3	SiO_2	Fe_2O_3	TiO_2	Na_2O	CaO	S_{Total}
37.87	23.56	2.58	4.02	15.32	0.10	0.64

Table 7 presents that many Na_2O and Al_2O_3 entered in the red mud. There are several possible explanations for this result. First, they may transfer to the solid phases containing sodium or aluminum. Second, aluminum may be lost due to incomplete reactions. Third, the entrainment loss is inevitable. Among them, the first two reasons have been verified by the XRD patterns of the red mud, as shown in Fig. 7.

Figure 7 reveals that the main components of the red mud were diaspore, sodalite, sodium aluminum silicate hydrate, lazurite, hematite (syn), erdite and iron sulfide. Sodalite, sodium aluminum silicate hydrate, hematite and lazurite were the typical components of red mud. Diaspore was usually originated from incomplete decomposition of the bauxite, but erdite and iron sulfide did not appear in the bauxite and were less reported in literature. These two substances may be from the recrystallization of sulfur and iron after the Bayer digestion. Further tests carried out with SEM−EDS confirmed this conjecture, as shown in Fig. 8.

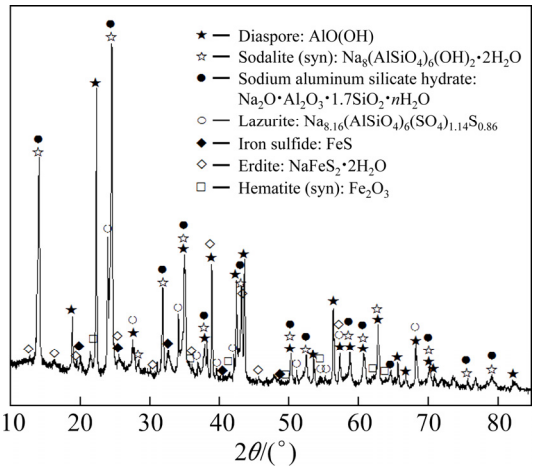

Fig. 7 XRD patterns of red mud

Figure 8 shows that the sulfur and iron in the red mud have similar distribution, but it should be mentioned that their contents are relatively low and dispersal. Compared with XRD patterns of the red mud, it can be inferred that the sulfur−iron compounds are fine particles. These fine particles are usually challenging to exist stably at such a high temperature of 543 K. Combined with XRD patterns of the bauxite in Fig. 4, there were no pronounced characteristic peaks of erdite and iron sulfide in the bauxite, so it also implied that sulfur

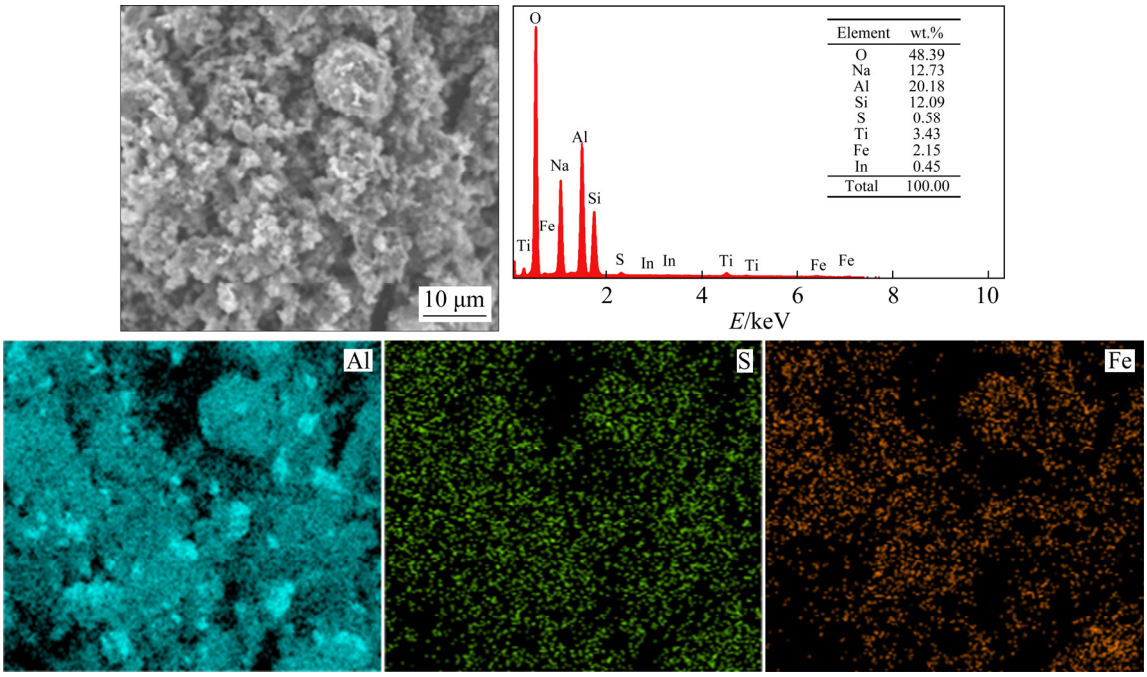

Fig. 8 Elemental mapping of red mud

was combined with iron to precipitate when the temperature decreased. In our previous research, a significant discovery was that as the sulfur content increased in the sodium aluminate solution, the iron content also increased, and FeS was found in the red mud [7].

However, it is necessary to highlight that the particles of the sulfur−iron compounds are very fine, resulting in the difficulty of precipitation and separation from the sodium aluminate solution. Therefore, it is impractical to remove iron and sulfur only by cooling operation, and the crystallization behavior of sulfur−iron compounds should be explored and studied in detail.

4.5 Crystallization behavior of sulfur−iron compounds in sodium aluminate solution

After standing of the bauxite leaching filtrate for 120 h, many dark green substances were observed at the bottom of the crystallizer, as shown in Fig. 9.

It is clear from Fig. 9(a) that the digestion solution of high-sulfur bauxite was dark black. After standing for 120 h, abundant dark green substances congregated at the bottom of the crystallizer, and the upper layer was the supernatant (see Fig. 9(b)). After removing the supernatant, the dark green substance was directly dried in an oven, since the particle was too fine to filter. Dried precipitate is displayed in Fig. 9(c). During the standing process, the conductivity of the solution and the content changes of sulfur and iron ion were analyzed, as shown in Fig. 10.

Figure 10(a) demonstrates no prominent induction period for the crystallization process of sulfur−iron compounds, and it can be roughly divided into two stages. The first stage (Zone I) is a nucleation stage with a sharp increase of conductivity depending on the standing time. Combined with Fig. 10(b), it is evident that the concentration of sulfur and iron in solution decreased markedly at this stage, and lots of sulfur−iron substances precipitated at the bottom of the crystallizer. Concurrently, the system was gradually changed into heterogeneous phases, and the conductivity significantly increased with prolonging the standing time. The second stage (Zone II) is a growth period. The ion concentration

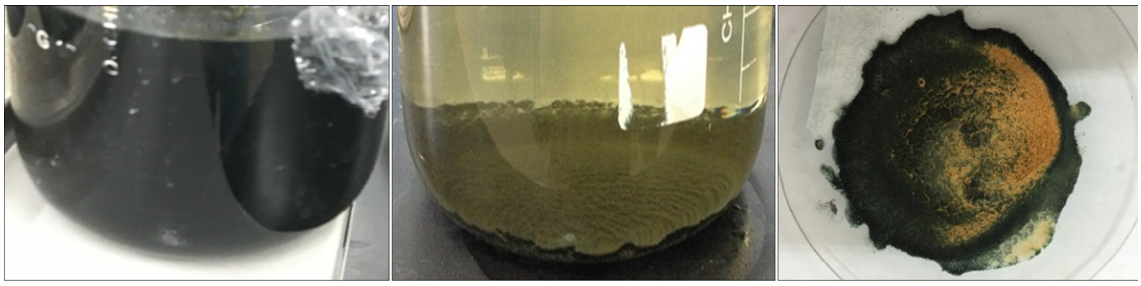

Fig. 9 Precipitation of sulfur and iron from sodium aluminate solution: (a) 0 h; (b) 120 h; (c) Precipitates

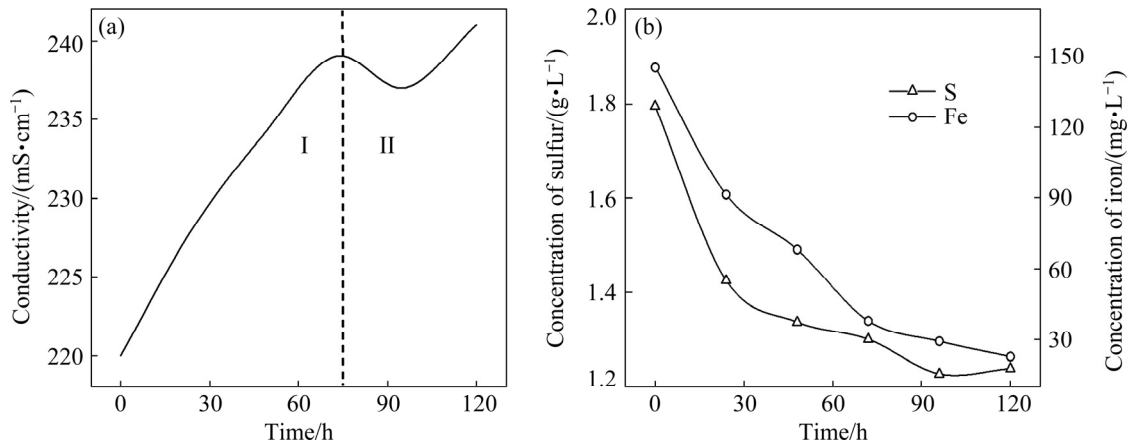

Fig. 10 Crystallization behavior of sulfur and iron in sodium aluminate solution: (a) Conductivity; (b) Concentration of sulfur and iron

of sulfur and iron in the solution continued to decrease, but the reduction rate was significantly slowed down. The conductivity of the system fluctuated slightly at this stage. These experimental results proved once again that the particles did not grow significantly. The dried dark green substance was analyzed by SEM, XRD and nano measurer 1.2, as displayed in Fig. 11 and Table 8.

As displayed in Fig. 11(a) and Table 8, the main elements of the dark green substance were O, Na, Al, Si, S and Fe. Although the sodium content of this substance seemed to be very high, AAS analysis manifested that the sodium concentration before and after precipitation was almost unchanged. The contents of Fe, C and S in the dark green substance were 2.43%, 12.23% and 4.56%, respectively. Figures 11(b, c) implied that the dark green substance was composed of many fine particles, and about 90% of the particle size was concentrated between 2 and 12 μm. In addition, as a result of the agglomeration, the measured particle size was much larger than its actual particle size, which was consistent with the phenomenon observed in the experiment. XRD analysis in Fig. 11(d) suggested that the compositions of this substance were sodium aluminum hydroxide hydrate, erdite, sodium iron oxide, pyrite, hematite, natrite (syn), etc, in which natrite (syn) was formed by the reaction of NaOH and CO_2 in the drying process.

Adding seed can effectively reduce the energy barrier of nucleation and intensify the simultaneous removal of sulfur and iron. Based on the thermodynamic analysis and experimental results, a novel process involving induced crystallization and reactive crystallization was adopted to simultaneously remove sulfur and iron from the digestion solution of high-sulfur bauxite.

4.6 Simultaneous removal of sulfur and iron from sodium aluminate solution

In the earlier published work, our research group has devoted to studying the simultaneous removal of sulfur and iron from the digestion solution of high-sulfur bauxite [8]. Pyrite (Fe 46.37%, S 50.07%) was used to prepare the sulfur−iron seed for increasing ion concentration. In the seed preparation and impurities removal process, a plastic wrap was covered on the crystallizer to reduce the negative influence of evaporation and

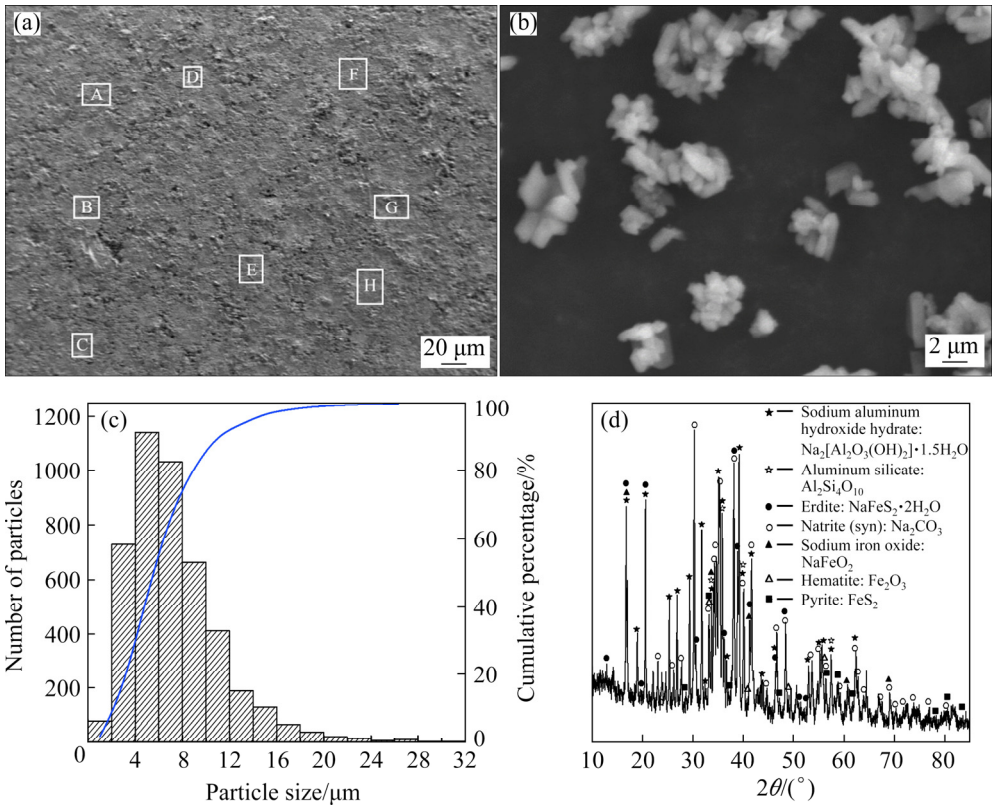

Fig. 11 Characteristics of dark green substance: (a) SEM image of pressed powder sample; (b) SEM image of powder sample; (c) Particle size distribution; (d) XRD pattern

Table 8 SEM−EDS analysis results for pressed powder of dark green substance in Fig. 11(a) (wt.%)

Zone	O	Na	Al	Si	S	Fe
A	50.8	28.26	6.5	5.95	5.84	1.17
B	47.83	18.63	12.71	12.11	6.54	1.79
C	49.68	39.38	2.97	2.52	1.8	1.43
D	50.24	32.5	5.06	5.78	3.96	2.46
E	43.95	40.7	0.69	1.14	5.69	2.49
F	44.63	37.48	0.77	1.08	5.14	4.92
G	50.31	28.47	8.19	7.54	3.79	1.71
H	46.96	13.73	21.72	11.64	0.51	2.12
Average	48.05	29.89	7.33	5.97	4.16	2.26

oxidation. The results suggested that the simultaneous removal ratios of sulfur and iron were significantly improved from 25% and 24% to 66% and 72% by adding seed slurry, respectively, and the loss of alumina was almost unchanged with values lower than 2% [8]. More details have been described in the previously published work [8].

In summary, thermodynamic analysis and experimental results manifest that the synergistic effect of induced crystallization and reactive crystallization can effectively reduce the sulfur and iron from the digestion solution of high-sulfur bauxite.

5 Conclusions

(1) When FeS_2 reacts with Na_2O_k at elevated temperature, iron prefers to enter in the slag as Fe_3O_4 and Fe_2O_3, and a small proportion of iron transfers into the solution as $Fe(OH)_3^-$, $HFeO_2^-$, $Fe(OH)_4^-$ and $Fe(OH)_4^{2-}$. Sulfur exists in the solution principally as S^{2-}, followed by SO_4^{2-}, and then SO_3^{2-} and $S_2O_3^{2-}$.

(2) In the cooling process, sulfur can combine with iron to precipitate as solids. φ_h−pH diagram of S−Fe−H_2O was constructed to clarify the predominant areas of sulfur−iron solids. Adding iron and metastable sulfur ions, decreasing temperature and controlling low potential are helpful to enlarging their predominance region and removing sulfur from the solution. Moreover, thermodynamics indicates that the predominant special species is $NaFeS_2·2H_2O$ rather than $NaFeS_2$.

(3) The experimental results are in good agreement with the thermodynamic analysis. In the leachate of high-sulfur bauxite, sulfur existed mainly as S^{2-}, which has exceeded 80% of the total sulfur content. The total iron concentration in the sodium aluminate solution is much higher than that of the normal alumina production process, in which more than 90% iron exists as Fe(II). Meanwhile, it is worth noting that sulfur−iron solids with fine particle size, such as $NaFeS_2·2H_2O$, FeS and FeS_2, frequently appear in red mud and precipitates of sulfur and iron solution.

(4) Thermodynamic analysis and experiments show that the synergistic effect of induced crystallization and reactive crystallization can effectively reduce sulfur and iron from sodium aluminate solution.

Acknowledgments

The authors are grateful for the financial supports from the National Natural Science Foundation of China (No. 51904052), the Chongqing Research Program of Basic Research and Frontier Technology, China (No. cstc2020jcyj-msxmX0476), the Science and Technology Research Program of Chongqing Municipal Education Commission, China (No. KJQN201901508), and the Graduate Science and Technology Innovation Training Program of Chongqing University of Science and Technology, China (No. YKJCX2020201).

Appendix

Appendix A−C in this work can be found at: http://www.ysxbcn.com/download/TNMSC-22-p2046-2021-0404-Appendix.pdf.

References

[1] LE T X, JU S H, LU L M, PENG J H, ZHOU L X, WANG S X. A novel process and its mechanism for recovering alumina from diasporic bauxite [J]. Hydrometallurgy, 2017, 169: 124−134.

[2] LI Xiao-bin, NIU Fei, LIU Gui-hua, QI Tian-gui, ZHOU Qiu-sheng, PENG Zhi-hong. Effects of iron-containing phases on transformation of sulfur-bearing ions in sodium aluminate solution [J]. Transactions of Nonferrous Metals Society of China, 2017, 27: 908−916.

[3] WU Hong-fei, CHEN Chao-yi, LI Jun-qi, LAN Yuan-pei, WANG Lin-zhu, QUAN Bian-li, JIN Hui-xin. Digestion mechanism and crystal simulation of roasted low-grade high-sulfur bauxite [J]. Transactions of Nonferrous Metals Society of China, 2020, 30: 1662−1673.

[4] CHEN Wen-mi, CHEN Xue-gang, GUO Jin-quan, HUANG Wei-guang, HU Xiao-lian. Research on the behavior of iron

in Bayer liquor [J]. Light Metals, 2008(4): 17−21. (in Chinese)

[5] DENG Yong-qin, WANG Xian-yong. Exploration and practice of Nanchuan bauxite in Bayer process [C]//The 2nd Non-ferrous Metals Industry Development Forum in the Midwest. Chongqing. 2009: 140−143. (in Chinese)

[6] HU Xiao-lian. Study on the behavior of sulfur during the digestion process of high sulfur-containing bauxite and on the process of sulfur removal [D]. Changsha: Central South University, 2011. (in Chinese)

[7] ZHOU Xue-jiao, CHEN Yong-li, YIN Jian-guo, XIA Wen-tang, YUAN Xiao-li, XIANG Xiao-yan. Study on Bayer digestion behaviour of low grade bauxite with high sulphur [J]. International Journal of Microstructure and Materials Properties, 2018, 13(3/4): 173−184.

[8] ZHOU Xue-jiao, YIN Jian-guo, CHEN Yong-li, XIA Wen-tang, XIANG Xiao-yan, YUAN Xiao-li. Simultaneous removal of sulfur and iron by the seed precipitation of digestion solution for high-sulfur bauxite [J]. Hydrometallurgy, 2018, 181: 7−15.

[9] JIN Chuang-shi, ZHANG Ting-an, MOU Wang-zhong, ZENG Yong, LIU Yan, LV Guo-zhi, JIANG Xiao-li. *E*−pH diagram of FeS_2−FeAsS−H_2O system for leaching pretreatment of refractory gold ore [J]. Journal of Materials and Metallurgy, 2011, 10(2): 120−124. (in Chinese)

[10] BOUET J, BRENET J P. Contribution a l'etude du diagramme tension/pH du fer en milieux sulfures [J]. Corrosion Science, 1963, 3(1): 51−63.

[11] LV Guo-zhi. Basic research on alumina production by using high-sulfur bauxite [D]. Shenyang: Northeastern University, 2010. (in Chinese)

[12] LI Xiao-bin, LI Chong-yang, QI Tian-gui, ZHOU Qiu-sheng, LIU Gui-hua, PENG Zhi-hong. Reaction behavior of pyrite during Bayer digestion at high temperature [J]. The Chinese Journal of Nonferrous Metals, 2013, 23(3): 829−835. (in Chinese)

[13] LIU Zhan-wei, YAN Heng-wei, MA Wen-hui, XIE Ke-qiang, XU Bao-qiang, ZHENG Li-cong. Digestion behavior and removal of sulfur in high-sulfur bauxite during Bayer process [J]. Minerals Engineering, 2020, 149(2): 106237.

[14] LIU Zhan-wei, YAN Heng-wei, MA Wen-hui, XIONG Ping. Sulfur removal of high-sulfur bauxite [J]. Mining, Metallurgy & Exploration, 2020, 37: 1617−1626.

[15] LIU Zhan-wei, MA Wen-hui, YAN Heng-wei, XIE Ke-qiang, LI Dun-yong, ZHENG Li-cong, LI Peng-fei. Removal of sulfur by adding zinc during the digestion process of high-sulfur bauxite [J]. Scientific Reports, 2017, 7(1): 17181.

[16] LIU Zhan-wei, YAN Heng-wei, MA Wen-hui, XIE Ke-qiang, LI Dun-yong, ZHENG Li-cong, LI Peng-fei. Sulfur removal by adding iron during the digestion process of high-sulfur bauxite [J]. Metallurgical & Materials Transactions B, 2018, 49B: 509−513.

[17] POUND B G, WRIGHT G A, SHARP R M. Electrochemical phase diagrams for the Fe/S/H_2O system under geothermal conditions [J]. Australian Journal of Chemistry, 1985, 38(5): 643−657.

[18] FERREIRA M G S, MELENDRES C A. Electrochemical and optical techniques for the study and monitoring of metallic corrosion [M]. Berlin: Springer Netherlands, 1991.

[19] CHEN Dai-geng, ZENG Zhi-gang, ZHAI Bin, YIN Xue-bo, ZHANG Guo-liang, OUYANG He-gen. Pourbaix diagrams and geological implications of Fe−S−H_2O hydrothermal system near 13°N on the east pacific rise [J]. Marine Geology & Quaternary Geology, 2010(2): 9−15. (in Chinese)

[20] WANG Ji-kun, LI Cun-xiong, LI Yong, ZHANG Hong-yao, HUANG Hui, YAN Jiang-feng, LIU Lu, WEI Chang. The *E*−pH figure of ZnS−FeS−H_2O system during acid leaching under pressure of high Iron sphalerite [J]. Nonferrous Metals (Smelting Part), 2006(2): 2−5. (in Chinese)

[21] XU Ying-peng, LI Jun-qi, CHEN Chon-yi, LAN Yuan-pei, LIU Long. Complex desulfurization during optimized digestion process of high-sulfur bauxite [J]. Nonferrous Metals (Extractive Metallurgy), 2018(12): 8−12. (in Chinese)

[22] LIU Long, LI Jun-qi, CHEN Chon-yi, LIU Li, WEI Guo-ling. Effect of ZnO addition on desulfurization process of high sulfur bauxite optimal conditions [J]. Nonferrous Metals (Extractive Metallurgy), 2017(1): 28−31. (in Chinese)

[23] LI Xiao-bin, NIU Fei, TAN Jie, LIU Gui-hua, QI Tian-gui, PENG Zhi-hong, ZHOU Qiu-sheng. Removal of S^{2-} ion from sodium aluminate solutions with sodium ferrite [J]. Transactions of Nonferrous Metals Society of China, 2016, 26: 1419−1424.

[24] LI Gang, XIN Yun-tao, LV Xiao-dong, TIAN Qing-hua, YAN Kang, YE Long-gang. Stability constants of Sb^{5+} with Cl^- and thermodynamics of Sb−S−Cl−H_2O system involving complex behavior of Sb with Cl [J]. Transactions of Nonferrous Metals Society of China, 2020, 30: 3379−3389.

[25] LIU Xiao-liang, XU Bin, YANG Yong-bin, LI Qian, JIANG Tao, HE Ying-he. Thermodynamic analysis of ammoniacal thiosulphate leaching of gold catalysed by Co(III)/Co(II) using E_h−pH and speciation diagrams [J]. Hydrometallurgy, 2018, 178: 240−249.

[26] XIAO Chao, ZENG Li, WEI Jia-hua, XIAO Lian-sheng, ZHANG Gui-qing. Thermodynamic analysis for the separation of tungsten and aluminum in alkaline medium using solvent extraction [J]. Hydrometallurgy, 2017, 174: 91−96.

[27] KATARZYNA S, SŁAWOMIR S, SIMON H. Modified multi-phase stability diagrams: An AMD case study at a site in Northumberland, UK [J]. Mine Water & the Environment, 2013, 32: 185−194.

[28] PEREZ-LABRA M, ROMERO-SERRANO A, SALINAS-RODRIGUEZ E, ÄVILA-DÄVILA E O, JUAREZ-LOPEZ G, HERNÄNDEZ-ÄVILA J. Kinetic and thermochemical analysis of rubidium jarosite decomposition in alkaline media [C]// WANG Shi-jie, DUTRIZAC J E, FREE M L, HWANG J Y, KIM D. TMS 2012. Amelia Gómez Villar, TMS, 2012: 447−460.

[29] SONG Yong-hui, HAHN H H, HOFFMANN E. Effects of solution conditions on the precipitation of phosphate for recovery: A thermodynamic evaluation [J]. Chemosphere, 2002, 48(10): 1029−1034.

[30] TREMAINE P R, LEBLANC J C. The solubility of magnetite and the hydrolysis and oxidation of Fe^{2+} in water to 300 °C [J]. Journal of Solution Chemistry, 1980, 9(6): 415−442.

[31] YANG Xian-wan. Thermodynamics data of inorganic substances in high temperature solution [M]. Beijing:

Metallurgical Industry Press, 1983. (in Chinese)
[32] BEVERSKOG B, PUIGDOMENECH I. Revised Pourbaix diagrams for iron at 25−300 °C [J]. Corrosion Science, 1996, 38(12): 2121−2135.
[33] LIU Zhan-wei, LI Dun-yong, MA Wen-hui, YAN Heng-wei, XIE Ke-qiang, ZHENG Li-cong, LI Peng-fei. Sulfur removal by adding aluminum in the Bayer process of high-sulfur bauxite [J]. Minerals Engineering, 2018, 119: 76−81.
[34] LASSIN A, PIANTONE P, CROUZET C, BODÉNAN F, BLANC P. Estimated thermodynamic properties of $NaFeS_2$ and erdite ($NaFeS_2$:$2H_2O$) [J]. Applied Geochemistry, 2014, 45: 14−24.
[35] BARD A J, PARSONS R, JORDAN J. Standard potentials in aqueous solution [M]. New York: Routledge, 1985.
[36] BARIN I. Thermochemical Data of Pure Substances [M]. 3rd ed. Weinheim: VCH, 2008.
[37] CHASE M W. NIST-JANAF thermochemical tables. Journal of physical and chemical reference data [M]. New York: American Chemical Society, 1998.
[38] WU Yan, PAN Xiao-lin, HAN Yue-jiao, YU Hai-yan. Dissolution kinetics and removal mechanism of kaolinite in diasporic bauxite in alkali solution at atmospheric pressure [J]. Transactions of Nonferrous Metals Society of China, 2019, 29: 2627−2637.
[39] ZHANG Shu-chao. Modern metallurgical analysis of light metal [M]. Beijing: Chemical Industry Press, 2007. (in Chinese)
[40] CHEN Wen-mi, HU Qin. Research on the analysis of low-valence sulphion in sodium aluminate solution [J]. Light Metals, 2012(10): 17−20. (in Chinese)
[41] TIAN Zhen. Discussion on iron and sulfur enrichment and treatment during Dressing Bayer process [J]. Light Metals, 2012(1): 12−19. (in Chinese)
[42] CHEN Xiao-jing. Influence of iron and sulfur enrichment on Bayer process system and its countermeasures [J]. Light Metals, 2011(S): 83−85. (in Chinese)
[43] XIE Qiao-ling, CHEN Wen-mi. Corrosion behavior of 16Mn low alloy steel in sulfide-containing Bayer solutions [J]. Corrosion Science, 2014, 86: 252−260.
[44] XIE Qiao-ling, CHEN Wen-mi. Effect of S^{2-} on corrosion behavior of low alloy steel in sodium aluminate solution [J]. The Chinese Journal of Nonferrous Metals, 2013(12): 3462−3469. (in Chinese)
[45] QUAN Bian-li, LI Jun-qi, CHEN Chao-yi. Effect of additional sulfide and thiosulfate on corrosion of Q235 carbon steel in alkaline solutions [J]. International Journal of Corrosion, 2016(7): 1−8.
[46] HAZLEWOOD P E, SINGH P M, HSIEH J S. Corrosion behavior of carbon steels in sulfide- containing caustic solutions [J]. Industrial & Engineering Chemistry Research, 2006, 45(23): 7789−7794.
[47] CHASSE K R, SINGH P M. Corrosion study of super ferritic stainless steel UNS S44660 (26Cr−3Ni−3Mo) and several other stainless steel grades (UNS S31603, S32101, and S32205) in caustic solution containing sodium sulfide [J]. Metallurgical and Materials Transactions A−Physical Metallurgy and Materials Science, 2013, 44: 5039−5053.
[48] LIU Gui-hua, GAO Jun-li, LI Xiao-bin, XU Shuang. Study on variation rule of iron in the aluminate solution after digestion process at high temperature by Bayer process [J]. Mining and Metallurgical Engineering, 2007, 27(5): 38−40. (in Chinese)

拜耳法 Na−S−Fe−H_2O 系热力学分析

周雪娇，谭 飞，陈永利，尹建国，夏文堂，黄青云，高绪东

重庆科技学院 冶金与材料工程学院，重庆 401331

摘 要：构建 Na−S−Fe−H_2O 系热力学图，分析拜耳法生产过程中硫和铁的行为。溶出后，铁最可能以 Fe_3O_4 和 Fe_2O_3 的形式进入赤泥，部分铁以 $Fe(OH)_3^-$、$HFeO_2^-$、$Fe(OH)_4^-$和 $Fe(OH)_4^{2-}$的形式转入液相。硫的优势物种是 S^{2-}，其次是 SO_4^{2-}，然后是 SO_3^{2-}和 $S_2O_3^{2-}$。热力学分析结果与实验测得的溶液中铁和硫的形态分布一致。当温度降低时，硫和铁会结合析出。控制低电位和降低温度均有利于将硫和铁从溶液中脱除。XRD 谱表明，$NaFeS_2{\cdot}2H_2O$、FeS 和 FeS_2 广泛存在于赤泥以及黄铁矿和高硫铝土矿溶出液的析出物中。热力学分析可用于指导拜耳法同步除硫和铁。

关键词：高硫铝土矿；Na−S−Fe−H_2O 系；热力学分析；同步脱除；硫；铁；拜耳法

(Edited by Bing YANG)